Accurate SiC MOSFET Chip V_{gs} Extraction Based on Parasitic Parameter Impact Compensation

Yang Li, *Student Member, IEEE*, Yuan Gao, Yan Zhang, *Member, IEEE*, Jinjun Liu, *Fellow, IEEE*, and Cheng Nie, *Member, IEEE*

***Abstract*—With the growing use of SiC MOSFET in power electronic equipment, it is meaningful to extract precise typical waveforms and characteristics for device manufacture, converter design, and operating evaluation. Many solutions have been proposed to improve measurement precision by equipment and essential techniques. However, the measured object should also be accurately identified as the existing measurement result consisting of the expected gate-source voltage (v_{GS}) and voltage drops on parasitic parameters between measuring points. This article, first, reveals the v_{GS} measurement deviation of TO-247-4 and TO-247-3 devices during the switching process and crosstalk, based on the equivalent circuit model and simulation waveforms. According to the clarification of the measured object, an improved v_{GS} extraction method is proposed to eliminate this deviation. Voltage drops on parasitic parameters are compensated, with the help of high-precision equipment and the proven parasitic parameter extraction technique. Experiments are constructed to verify the analysis of measurement deviation and the availability of the proposed method. Comparison between various operating conditions emphasizes its necessity, especially in high-capacity and low-driving-resistor applications, contributing to characterization, operating condition monitoring, protection design, and measurement understanding of wide band-gap devices.**

***Index Terms*—Gate-source voltage (v_{GS}) extraction, measurement deviation, parasitic parameter, silicon carbide (SiC) MOSFET, voltage drop compensation.**

I. Introduction

POWER electronic converters are widely used in electrical systems, where one of the core components is the power semiconductor device. To pursue higher efficiency and power density, wide band-gap devices such as SiC MOSFETs are widely used in power electronic equipment [1], [2], [3]. It is essential to acquire their switching characteristics for device manufacture, converter design, and equipment operating condition evaluation. It relies on accurate waveforms of i_{DS}, v_{DS}, and v_{GS} on the chip measured by a double pulse test (DPT). However, since SiC MOSFETs usually operate with a higher frequency than Si devices, measuring results of SiC devices more severely deviate from expected values on the chip. Test results not accurately reflecting devices' operating conditions have become a pending problem in research and engineering, which challenges their dynamic characterization.

Numerous studies have discussed methods to improve the precision of measurement in traditional DPT, which mainly focus on essential techniques and equipment selection [4], [5], [6], [7]. Gao and Chen [5] and Tektronix [8] indicated that the higher switching frequency requires a measuring system consisting of probes and an oscilloscope with enough bandwidth and a high sampling rate. Zhang et al. [4], Gao and Chen [5], and Keysight Technologies [9] analyzed voltage probes meeting the requirements of high bandwidth and sufficient dynamic range, whereas, Zhang et al. [4], Gao and Chen [5], and Witcher [6] gave a comprehensive comparison between different current measurement solutions. There is also research about grounding and propagation delays of probes. Techniques for ground lead parasitic inductance elimination have been proposed [5], [6], [8], [13], and a detailed V-I time alignment process has been concluded [4], [7]. Zeng et al. [10], [11], [12] even modeled measurement error induced by nonideal probes, providing theoretical support for probe selection. Based on the abovementioned discussion, Gao and Chen [5] gave a systematic summary to address improved techniques for measurement challenges by combining the latest measuring equipment.

Besides the precision of measurement, the higher switching frequency also challenges the accuracy, which has not got enough attention yet. As shown in Fig. 1, high precision means the results of multiple measurements are concentrated. However, a better measuring result also requires a low average deviation from the truth, whose premise is the accurate identification of the measuring object. Fig. 2 shows two common packages including TO-247-3 and TO-247-4, which represent the traditional package with 3 pins and the developed package with the kelvin source pin. According to equivalent circuits illustrated in Fig. 3, L_G, L_S, L_{KS}, and L_D represent the parasitic inductance induced by corresponding bonding wires and pins, and $R_{G(int)}$ is the intrinsic gate resistance. The voltages on these package-internal parasitic parameters are inevitably measured as

Manuscript received 6 September 2022; accepted 27 October 2022. Date of publication 11 November 2022; date of current version 26 December 2022. This work was supported in part by the National Key Research and Development Program of China under Grant 2021YFB2601500, in part by the National Natural Science Foundation of China under Grant 51807152, and in part by the State Key Laboratory of Electrical Insulation and Power Equipment. Recommended for publication by Associate Editor M. Wang. *(Corresponding authors: Yan Zhang; Jinjun Liu.)*

Yang Li, Yan Zhang, and Jinjun Liu are with the School of Electrical Engineering, Xi'an Jiaotong University, Xi'an 710049, China (e-mail: liyang.9710@stu.xjtu.edu.cn; zhangyanjtu@xjtu.edu.cn; jjliu@mail.xjtu.edu.cn).

Yuan Gao is with the Global Power Technology Co., Ltd., Beijing 100089, China (e-mail: gerryyuan@foxmail.com).

Cheng Nie is with the TBEA Co., Ltd., Xi'an 710117, China (e-mail: nie-cheng@163.com).

Color versions of one or more figures in this article are available at https://doi.org/10.1109/TPEL.2022.3221640.

Digital Object Identifier 10.1109/TPEL.2022.3221640

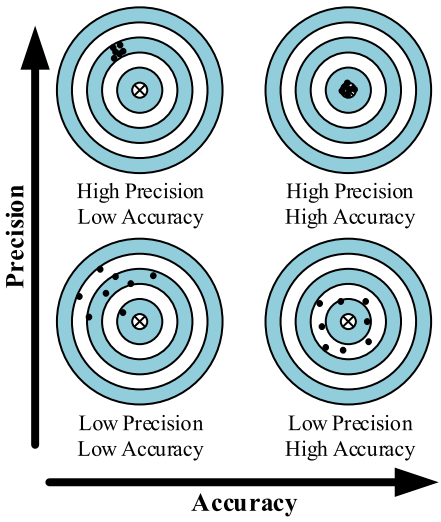

Fig. 1. Two dimensions of measurement evaluation.

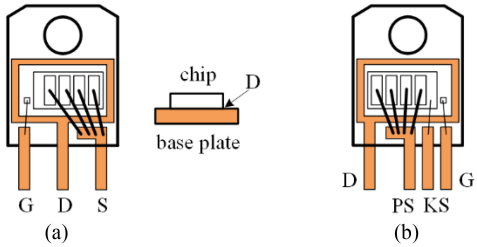

Fig. 2. Internal structure of SiC MOSFET. (a) TO-247-3. (b) TO-247-4.

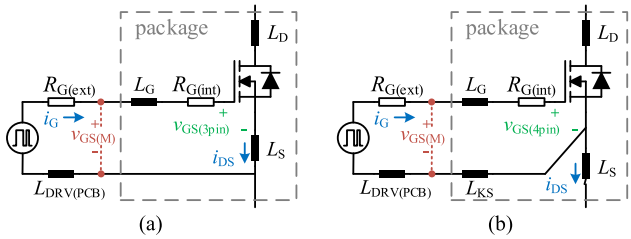

Fig. 3. Equivalent circuit of SiC MOSFET. (a) TO-247-3. (b) TO-247-4.

a part of v_{DS} or v_{GS}. The measurement deviation is acceptable and not obvious in v_{DS}. However, v_{GS} in normal operation is usually as low as only −5–20 V, whose measurement deviation cannot be neglected. It is widely acknowledged that v_{GS} on the chip ($v_{GS(3pin)}$/$v_{GS(4pin)}$) is expected to reflect the dynamic characteristics of devices. In most instances, v_{GS} on the package ($v_{GS(M)}$) is measured to represent it for convenience. However, they are quite different when discussing the SiC MOSFET. Among these package-internal parasitic parameters in Fig. 3, L_G, L_S (or L_{KS}), and $R_{G(int)}$ are between measuring points of v_{GS} in the TO-247-3 (or TO-247-4) package, inducing the deviation between $v_{GS(M)}$ and $v_{GS(3pin)}$ ($v_{GS(4pin)}$). Although L_G and L_S (or L_{KS}) between measuring points can be eliminated as much as possible [14], these parasitic parameters between measuring points of v_{GS} still generate a considerable voltage drop.

Many studies have modeled the parasitic parameter impact on nonideal switching characteristics [15], [16], [17], [18], [19], [20], but few of them pay attention to the deviation of the v_{GS} measuring object. Studies about the crosstalk focus on modeling [21], [22], [23] and suppression [24], [25], [26], [27] methods, where the v_{GS} on the chip is analyzed. The confusion of $v_{GS(M)}$ and $v_{GS(3pin)}$/$v_{GS(4pin)}$ in experiments may mislead the analysis and verification of models and suppression methods. To minimize the test error, external driving resistance is selected as 5–10 times the normal value in practice in [23], which is meaningless for guiding practical applications. Li et al. [27] has been aware of the severe deviation between measurement and analysis, but have not given a detailed analysis and a complete correction method. v_{GS} measurement deviation induced by a common source inductor (CSI) has been discussed in [28], and a potential solution is to adopt packages decoupling the driving circuit and the main circuit. Although CSI is eliminated, the effect of other parasitic parameters between v_{GS} measuring points still exists, which means the problem is still not fundamentally solved. It is essential to accurately identify the v_{GS} measuring object, otherwise, studies for improving the precision of measurement equipment will be meaningless. Therefore, an extraction method for exact v_{GS} on the chip is urgent and meaningful for dynamic characterization and driving circuit design.

This article aims to analyze the v_{GS} measurement deviation caused by parasitic parameters between measuring points, and propose a method to extract the accurate v_{GS} on the chip from the measured one. Other parts are organized as follows. The impact of parasitic parameters between measuring points on v_{GS} measurement during the switching process and crosstalk is illustrated in Sections II and III. Section IV proposes a more accurate v_{GS} extraction method with specific steps. In Section V, a DPT experiment is constructed for verification, and different operating conditions are tested and discussed. Finally, Section VI concludes this article.

II. Impacts of Parasitic Parameters on v_{GS} Measurement During Switching Process

A. TO-247-4 Package

The typical switching process of SiC MOSFETs in common applications can be simplified as the half-bridge circuit with an inductive load. As shown in Fig. 4, L is the load inductor, C_{Bus} is the bus capacitor, L_{Loop} is the equivalent series inductance in the commutation circuit, Q_H and Q_L are the upper and lower SiC MOSFETs, and D_H and D_L are body diodes of them. Besides L_G, L_{KS}, and $R_{G(int)}$, there are also parasitic parameters including external driving resistor $R_{G(ext)}$, and the PCB-induced inductance $L_{DRV(PCB)}$. The gate signal is connected to the active device Q_L, whereas the complementary device Q_H keeps OFF. The load current I_L and the bus voltage V_{Bus} are considered constant during the switching process.

According to the Q_L control circuit in Fig. 4, the relationship between $v_{GS(M)}$ and $v_{GS(4pin)}$ always satisfies (1). The key is to analyze the significant difference between them during the switching process. Fig. 5(a) shows typical turn-ON waveforms of Q_L. Before t_0, both Q_L and Q_H are in the OFF state, thus,

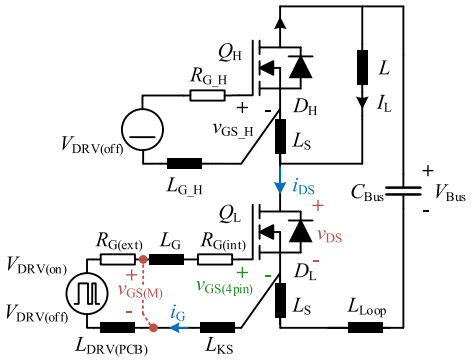

Fig. 4. Switching process equivalent circuit of TO-247-4 SiC MOSFET.

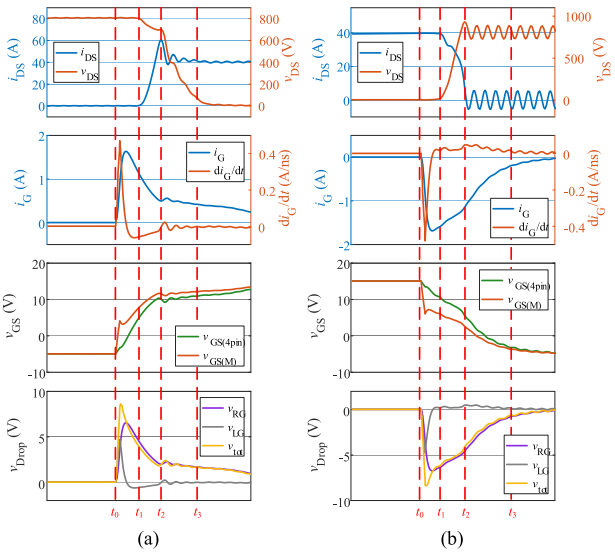

Fig. 5. Switching process of TO-247-4 SiC MOSFET (Simulation based on IMZ120R045M1 devices, $I_L = 40$ A, $V_{Bus} = 800$ V, $V_{DRV(ON)} = 15$ V, $V_{DRV(OFF)} = -5$ V, and $L = 100$ μH). (a) Turn ON. (b) Turn OFF.

$v_{GS(4pin)} = V_{DRV(OFF)}$, $v_{GS\_H} = V_{DRV(OFF)}$, $i_{DS} = 0$A, and $v_{DS} = V_{Bus}$. The turn-ON process is divided into three stages [28]

$$v_{GS(M)} = v_{GS(4pin)} + i_G \cdot R_{G(int)} + (L_G + L_{KS}) \cdot \mathrm{d}i_G/\mathrm{d}t. \quad (1)$$

Stage 1 [$t_0 \le t < t_1$]: At t_0, the driving voltage rapidly changes from $V_{DRV(OFF)}$ to $V_{DRV(ON)}$, and C_{iss} consisting of C_{GS} and C_{GD} is charged by i_G. Since $v_{GS(4pin)}$ does not reach the threshold voltage $V_{GS(th)}$, Q_L is still in the OFF state and v_{DS} keeps as V_{Bus}, which makes C_{iss} constant and $\mathrm{d}v_{GS}/\mathrm{d}t = \mathrm{d}v_{GD}/\mathrm{d}t$. This stage can be expressed by a second-order differential equation system shown as (2) and (3), where $R_{G(L)} = R_{G(int)} + R_{G(ext)}$ and $L_{G(L)} = L_G + L_{KS} + L_{DRV(PCB)}$. Since $L_{G(L)}$ is small enough [28], the quadratic differential term $L_{G(L)}C_{iss}$ is too smaller to be neglected when solving $v_{GS(4pin)}$, and it can be expressed as (4)

$$V_{DRV(ON)} = v_{GS(4pin)} + i_G \cdot R_{G(L)} + L_{G(L)} \cdot \mathrm{d}i_G/\mathrm{d}t \quad (2)$$

$$i_G = C_{iss} \cdot \mathrm{d}v_{GS(4pin)}/\mathrm{d}t \quad (3)$$

$$v_{GS(4pin)}(t) = V_{DRV(ON)} - (V_{DRV(ON)} - V_{DRV(OFF)})\mathrm{e}^{-\frac{t-t_0}{R_{G(L)} \cdot C_{iss}}}. \quad (4)$$

Since $L_{G(L)}$ is too small, i_G sharply increases, generating a significant voltage drop on L_G and L_{KS} (v_{LG}). It is measured as a part of $v_{GS(M)}$, making it dramatically rise almost to $V_{GS(th)}$. It deviates from $v_{GS(4pin)}$ and seriously misleads that Q_L starts to turn ON in advance. After that, i_G gradually drops, and the voltage drop on $R_{G(int)}$ (v_{RG}) dominates the measured deviation between $v_{GS(M)}$ and $v_{GS(4pin)}$, whereas the negative v_{LG} relieves it a little. As shown in Fig. 5(a) and (5), $v_{GS(M)}$ still keeps larger than $v_{GS(4pin)}$ even when $v_{GS(4pin)}$ reaches $V_{GS(th)}$ at t_1

$$v_{GS(M)} = v_{GS(4pin)} + \left(\frac{R_{G(int)}}{R_{G(L)}} - \frac{L_G + L_{KS}}{R_{G(L)}^2 \cdot C_{iss}}\right) \cdot (V_{DRV(ON)} - v_{GS(4pin)}). \quad (5)$$

Stage 2 [$t_1 \le t < t_2$]: When $v_{GS(4pin)}$ exceeds $V_{GS(th)}$, Q_L starts turning on and operates in the saturation region, and i_{DS} increases rapidly. Since v_{DS} seldom reduces, C_{iss} keeps constant and is still charged by i_G, which means that $v_{GS(4pin)}$ continues increasing until t_2, and still satisfies (4). The relationship in (5) still holds, and $v_{GS(M)}$ is still larger than $v_{GS(4pin)}$, which is mainly affected by v_{RG}.

Stage 3 [$t_2 \le t < t_3$]: At t_2, i_{DS} reaches the peak value, D_H starts turning OFF, and v_{DS} starts decreasing rapidly. C_{GD} significantly increases, causing almost the whole i_G to charge C_{GD}, even discharging C_{GS}. Thus, $v_{GS(4pin)}$ decreases, and i_G increases at first. After that, during the miller ramp stage [28], i_G charges both C_{GD} and C_{GS}. C_{GD} is significantly increasing during v_{DS} decrease, so $|i_G|$ declines much slower than during *Stage 1*. The declining v_{RG} is almost the whole reason for the measured deviation since the small $|\mathrm{d}i_G/\mathrm{d}t|$ generates almost no v_{LG}, and it makes $v_{GS(M)}$ increase slower than $v_{GS(4pin)}$.

After t_3, i_{DS}, and v_{DS} keep almost constant, Q_L operates out of the saturation region and the turn-ON process ends. $v_{GS(4pin)}$ gradually increases to reach $V_{DRV(ON)}$ and $|i_G|$ gradually decreases to 0. The relationship between $v_{GS(4pin)}$ and $v_{GS(M)}$ is still expressed by (5), with the enhanced C_{iss}.

The typical waveforms of the turn-OFF process are shown in Fig. 5(b). Before t_0, $v_{GS(4pin)}$ of Q_L is equal to $V_{DRV(ON)}$, and Q_L conducts I_L. D_H is in the OFF state, withstanding V_{Bus}. The turn-OFF process is divided into three stages, which is almost the inverse of the turn-ON process.

Stage 1 [$t_0 \le t < t_1$]: At t_0, the driving voltage rapidly changes from $V_{DRV(ON)}$ to $V_{DRV(OFF)}$. Since Q_L operates in the ohm region, i_{DS} and v_{DS} seldom change. C_{iss} is discharged by i_G and $v_{GS(4pin)}$ decrease, which can also be expressed by (3) and (6), and $v_{GS(4pin)}$ is solved, as expressed in (7)

$$V_{DRV(OFF)} = v_{GS(4pin)} + i_G \cdot R_{G(L)} + L_{G(L)} \cdot \mathrm{d}i_G/\mathrm{d}t \quad (6)$$

$$v_{GS(4pin)}(t) = V_{DRV(OFF)} - (V_{DRV(OFF)} - V_{DRV(ON)})\mathrm{e}^{-\frac{t-t_0}{R_{G(L)} \cdot C_{iss}}}. \quad (7)$$

Since $L_{G(L)}$ is too small, i_G sharply decreases and then gradually rises, corresponding that v_{LG} and v_{RG} dominate the

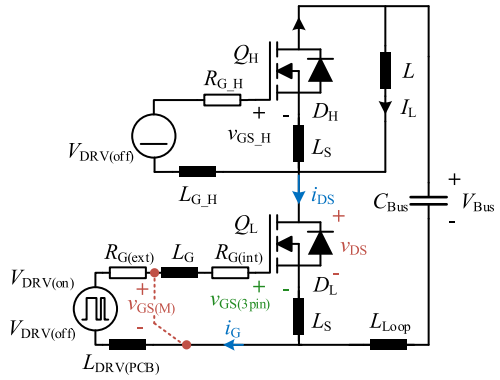

Fig. 6. Switching process equivalent circuit of TO-247-3 SiC MOSFET.

$v_{GS(M)}$ deviation from $v_{GS(4pin)}$. As shown in Fig. 5(b) and (8), this deviation is mainly expressed as the sharp drop at first, the smaller value, and the slower decrease. It seriously misleads that Q_L enters the saturation region in advance

$$v_{GS(M)} = v_{GS(4pin)} + \left(\frac{R_{G(int)}}{R_{G(L)}} - \frac{L_G + L_{KS}}{R_{G(L)}^2 \cdot C_{iss}}\right) \cdot (V_{DRV(OFF)} - v_{GS(4pin)}). \quad (8)$$

Stage 2 [$t_1 \le t < t_2$]: Q_L operates in the saturation region, and i_{DS} charges C_{DS} and C_{GD} to increase v_{DS}. Both $v_{GS(4pin)}$ and $|i_G|$ decrease during the miller ramp stage, making $v_{GS(M)}$ decrease slower and keep smaller than $v_{GS(4pin)}$. It seriously misleads that Q_L starts to turn OFF in advance.

Stage 3 [$t_2 \le t < t_3$]: At t_2, v_{DS} reaches V_{Bus}, and i_{DS} almost drops to 0, which means Q_L is in the OFF state. Both $v_{GS(4pin)}$ and $|i_G|$ continue to decrease as i_G discharges C_{iss}, and the relationship between $v_{GS(4pin)}$ and $v_{GS(M)}$ is still expressed by (8), with the reduced C_{iss}. Until t_3, $v_{GS(4pin)}$ declines to $V_{DRV(OFF)}$, and the turn-OFF process ends.

As analyzed previously, $v_{GS(M)}$ dramatically deviates from $v_{GS(4pin)}$ in *Stages 1* and *2* of both the turn-ON and turn-OFF process, severely misleads the judgment when Q_L starts to turn ON/OFF and to operate in the separation/ohm region.

B. TO-247-3 Package

Compared with the equivalent circuit of TO-247-4 devices, there is no L_{KS} but L_S in that of TO-247-3 devices, as shown in Fig. 6. The relationship between $v_{GS(M)}$ and $v_{GS(3pin)}$ always satisfies (9), which shows that CSI induces voltage drop into the control circuit caused by the power stage behavior di_{DS}/dt, deviating v_{GS} measurement. Thus, the obvious difference between the v_{GS} measurement of two kinds of packages during the switching process is in the i_{DS}-varying stages

$$v_{GS(M)} = v_{GS(3pin)} + i_G \cdot R_{G(int)} + (L_G + L_S) \cdot di_G/dt + L_S \cdot di_{DS}/dt. \quad (9)$$

During the turn-ON process, i_{DS} increases in *Stage 2* and oscillates at the beginning of *Stage 3*, as waveforms in Fig. 7(a) show. The rapidly rising i_{DS} in *Stage 2* generates a dramatical voltage drop v_{LS} on L_S, which raises $v_{GS(M)}$ to twice of $v_{GS(3pin)}$, even larger than $V_{DRV(ON)}$, and almost reaching the v_{GS} limit. The oscillating i_{DS} in *Stage 3* induces overestimated oscillation into $v_{GS(M)}$. It seriously misleads not only turn-ON characterization but also driving circuit design since $v_{GS(3pin)}$ is still safe enough in *Stage 2* and seldom oscillates in *Stage 3*.

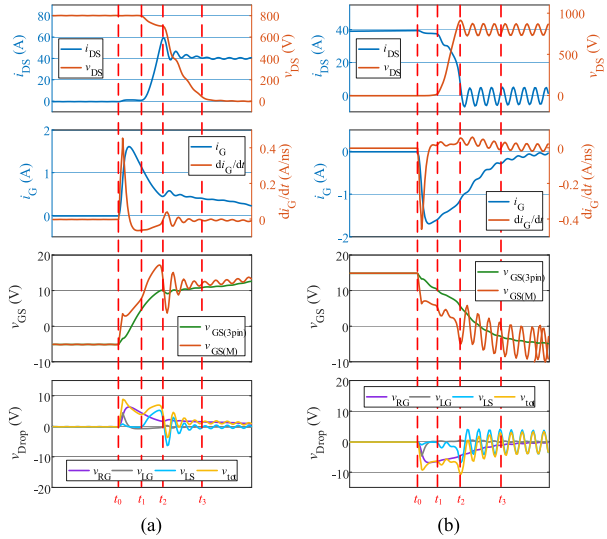

Fig. 7. Switching process of TO-247-3 SiC MOSFET (Simulation based on IMZ120R045M1 devices, $I_L = 40$ A, $V_{Bus} = 800$ V, $V_{DRV(ON)} = 15$ V, $V_{DRV(OFF)} = -5$ V, and $L = 100$ μH). (a) Turn ON. (b) Turn OFF.

During the turn-OFF process, i_{DS} decreases in *Stage 2* and oscillates in *Stage 3*, as waveforms in Fig. 7(a) show. The rapidly descending i_{DS} in *Stage 2* pulls $v_{GS(M)}$ down to close to 0 V. The oscillating i_{DS} in *Stage 3* generates voltage oscillation on L_S, amplifying $v_{GS(M)}$ oscillation. It seriously misleads not only turn-OFF characterization but also driving circuit design since the device still operates in the saturation region with enough $v_{GS(3pin)}$ in *Stage 2* and seldom oscillates in *Stage 3*.

It is emphasized that there is also a significant deviation in $v_{GS(M)}$ from $v_{GS(3pin)}$ induced by di_G/dt, which is almost the same as the TO-247-4 package and not elaborated.

III. Impacts of Parasitic Parameters on v_{GS} Measurement During Crosstalk

A. TO-247-4 Package

Parasitic parameters between measuring points also affect v_{GS} measuring results during the crosstalk, which is reflected in v_{GS} of the complementary device during the active device commutation process. Fig. 8 shows the crosstalk equivalent circuit of TO-247-4 devices. Compared with Fig. 4, the main difference is that the driving signal is added on the gate of Q_H, and crosstalk occurs on Q_L, which is the device under test for reliable grounding of measurement. Correspondingly, L is in parallel with Q_L. Thus, the relationship between $v_{GS(M)}$ and $v_{GS(4pin)}$ satisfies

$$v_{GS(M)} = v_{GS(4pin)} + i_G \cdot R_{G(int)} + (L_G + L_{KS}) \cdot di_G/dt. \quad (10)$$

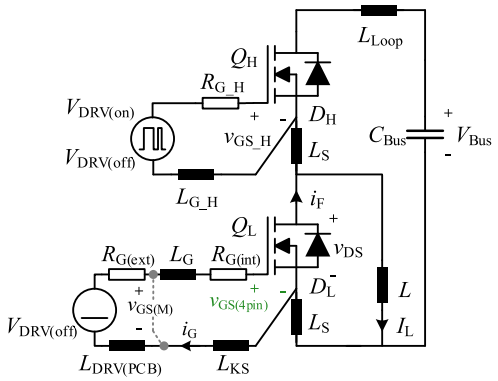

Fig. 8. Crosstalk equivalent circuit of TO-247-4 SiC MOSFET.

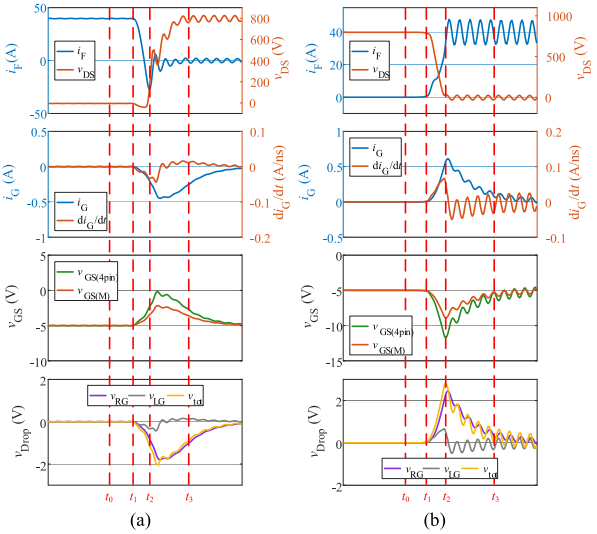

Fig. 9. Crosstalk of TO-247-4 SiC MOSFET (Simulation based on IMZ120R045M1 devices, $I_L = 40$ A, $V_{Bus} = 800$ V, $V_{DRV(ON)} = 15$ V, $V_{DRV(OFF)} = -5$ V, and $L = 100$ μH). (a) Turn ON. (b) Turn OFF.

Fig. 9(a) shows the typical crosstalk waveforms of Q_L during the Q_H turn-ON process. D_L enters in reverse recovery, and v_{DS} increases from V_F to V_{Bus}. Since v_{GS} of Q_L maintains $V_{DRV(OFF)}$, v_{DG} increases from V_F-$V_{DRV(OFF)}$ to V_{Bus}-$V_{DRV(OFF)}$, generating a displacement current through C_{GD}. It generates a voltage drop on $R_{G(L)}$ and $L_{G(L)}$, and charges C_{GS}. An upward spike of v_{GS} appears, as described by (11), which is turn-ON crosstalk occurring in *Stage 2* and *3* of the Q_H turn-ON process

$$v_{GS(4pin)} = V_{DRV(OFF)} + R_{G(L)} \cdot i_G + L_{G(L)} \cdot di_G/dt. \quad (11)$$

Stage 2 [$t_1 \le t < t_2$]: At t_1, i_F decreases from I_L, and v_{DS} increases from V_F. Although v_{DS} growth is slow and small, $v_{GS(4pin)}$ still obviously increases due to the large C_{GD}, and i_G generates a voltage drop on L_G, L_{KS}, and $R_{G(int)}$ opposite to $v_{GS(4pin)}$. Thus, $v_{GS(M)}$ is always smaller than $v_{GS(4pin)}$.

Stage 3 [$t_2 \le t < t_3$]: At t_2, D_L starts withstanding the reverse voltage, and v_{DS} rapidly increases. Although C_{GD} is decreasing, dv_{DS}/dt is large at first, so $v_{GS(4pin)}$ first increases and then decreases. After t_3, the turn-ON process of Q_H ends, C_{GS} is discharged and $v_{GS(4pin)}$ gradually declines to $V_{DRV(OFF)}$. Since the voltage drop on L_G, L_{KS}, and $R_{G(int)}$ is opposite to $v_{GS(4pin)}$, $v_{GS(M)}$ has a smaller peak amplitude than $v_{GS(4pin)}$.

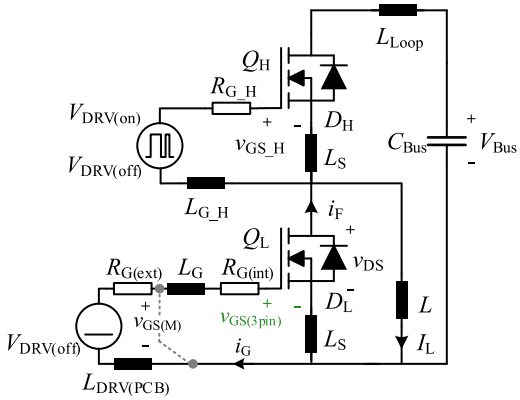

Fig. 10. Crosstalk equivalent circuit of TO-247-3 SiC MOSFET.

As shown in Fig. 9(b), the turn-OFF crosstalk is almost the inverse process of turn-ON crosstalk, which occurs in *Stage 2* and *3* of the Q_H turn-OFF process. D_L starts freewheeling, and v_{DS} decreases from V_{Bus} to V_F. v_{DG} decreases from V_{Bus}-$V_{DRV(OFF)}$ to V_F-$V_{DRV(OFF)}$, generating a displacement current through C_{GD}. It generates a voltage drop on $R_{G(L)}$ and $L_{G(L)}$, and discharges C_{GS}, causing a downward spike of v_{GS} described by (11).

Stage 2 [$t_1 \le t < t_2$]: At t_1, i_F starts increasing, and v_{DS} starts decreasing from V_{Bus}. Although C_{GD} is decreasing, dv_{DS}/dt is so large that $v_{GS(4pin)}$ decreases, and i_G generates a voltage drop on L_G, L_{KS}, and $R_{G(int)}$ opposite to $v_{GS(4pin)}$. Thus, $v_{GS(M)}$ is always smaller than $v_{GS(4pin)}$.

Stage 3 [$t_2 \le t < t_3$]: At t_2, D_L starts withstanding I_L, and v_{DS} reaches V_F. Q_H is in the OFF state, and C_{GS} is discharged with $v_{GS(4pin)}$ gradually back to $V_{DRV(OFF)}$, with oscillation induced by v_{DS}. Since the voltage drop on L_G, L_{KS}, and $R_{G(int)}$ is opposite to $v_{GS(4pin)}$, $v_{GS(M)}$ has a smaller peak amplitude than $v_{GS(4pin)}$.

Since i_G is generated by $v_{GS(4pin)}$-$V_{DRV(OFF)}$, $|i_G|$ first increases and then decreases during both turn-ON and turn-OFF crosstalk. The voltage drop on L_G, L_{KS}, and $R_{G(int)}$ opposite to $v_{GS(4pin)}$ makes $|v_{GS(M)}|$ always smaller than $|v_{GS(4pin)}|$, which means the voltage peaks during both turn-ON and turn-OFF crosstalk are measured conservatively, reducing the security of the design.

B. TO-247-3 Package

Based on the crosstalk equivalent circuit of TO-247-3 devices shown in Fig. 10, the relationship between $v_{GS(M)}$ and $v_{GS(4pin)}$ satisfies (12). Compared with TO-247-4 devices, CSI in TO-247-3 devices affects crosstalk waveforms, which satisfies (13) and has been amply explained in [28]. The induced voltage drop caused by di_F/dt also has significant impacts on measurement. As shown in Fig. 11, the obvious difference between the v_{GS} measurement of two packages during crosstalk is in

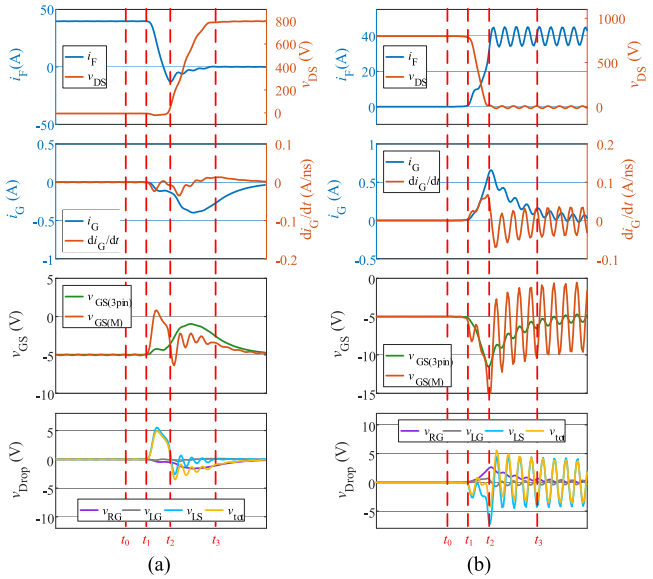

Fig. 11. Crosstalk of TO-247-3 SiC MOSFET (Simulation based on IMZ120R045M1 devices, $I_{\mathrm{L}} = 40$ A, $V_{\mathrm{Bus}} = 800$ V, $V_{\mathrm{DRV(ON)}} = 15$ V, $V_{\mathrm{DRV(OFF)}} = -5$ V, and $L = 100$ μH). (a) Turn ON. (b) Turn OFF.

the i_{F}-varying stages, which dominates the impacts of parasitic parameters on v_{GS} measurement

$$v_{\mathrm{GS(M)}} = v_{\mathrm{GS(3pin)}} + i_{\mathrm{G}} \cdot R_{\mathrm{G(int)}} + (L_{\mathrm{G}} + L_{\mathrm{S}}) \cdot \mathrm{d}i_{\mathrm{G}}/\mathrm{d}t - L_{\mathrm{S}} \cdot \mathrm{d}i_{\mathrm{F}}/\mathrm{d}t \quad (12)$$

$$v_{\mathrm{GS(3pin)}} = V_{\mathrm{DRV(OFF)}} + R_{\mathrm{G(L)}} \cdot i_{\mathrm{G}} + L_{\mathrm{G(L)}} \cdot \mathrm{d}i_{\mathrm{G}}/\mathrm{d}t - L_{\mathrm{S}} \cdot \mathrm{d}i_{\mathrm{F}}/\mathrm{d}t. \quad (13)$$

During the Q_{H} turn-ON process, i_{F} decreases in *Stage 2* and gradually increases with oscillation in *Stage 3*, as waveforms in Fig. 11(a) show. The rapidly descending i_{F} in *Stage 2* generates a dramatic voltage drop on L_{S}, which generates a downward spike as high as 5 V in $v_{\mathrm{GS(M)}}$. In *Stage 3*, the rapidly rising v_{DS} generates a downward spike in i_{G}, which generates a voltage drop on L_{G}, L_{S}, and $R_{\mathrm{G(int)}}$ opposite to $v_{\mathrm{GS(3pin)}}$. Meanwhile, the oscillating i_{F} generates a damping voltage drop with oscillation on L_{S}. The superposition of these two impacts causes $v_{\mathrm{GS(M)}}$ quite different from $v_{\mathrm{GS(3pin)}}$, especially misjudgment of the stage that the v_{GS} peak exists. It misleads crosstalk characterization and driving circuit design.

During the Q_{H} turn-OFF process, there are two pieces of rapid i_{F} rose in *Stage 2* and i_{F} oscillation in *Stage 3*, which generates voltage drop on L_{G}, L_{S}, and $R_{\mathrm{G(int)}}$. Thus, two downward spikes are superposed to $v_{\mathrm{GS(M)}}$ in *Stage 2*, and in-phase oscillation is superposed to $v_{\mathrm{GS(M)}}$ in *Stage 3*. The overestimated peak and oscillation in $v_{\mathrm{GS(M)}}$ mislead crosstalk characterization and driving circuit design.

It is emphasized that there is also a significant deviation in $v_{\mathrm{GS(M)}}$ from $v_{\mathrm{GS(3pin)}}$ induced by $\mathrm{d}i_{\mathrm{G}}/\mathrm{d}t$, which is almost the same as the TO-247-4 package and not elaborated.

IV. Improved v_{GS} Extraction Method

According to the former analysis, i_{G} and i_{DS} dramatically affect the measured v_{GS} of TO-247-4 and TO-247-3 devices, respectively, by voltage drop on parasitic parameters. In this part, an improved v_{GS} extraction method is proposed, with the main idea that the above voltage drop can be counteracted by measuring i_{G} and i_{DS}. Thus, based on Fig. 3, the extracted v_{GS} can be expressed by the measured v_{GS} plus a correction term, as described in (14) and (15), for TO-247-4 and TO-247-3 devices. Details of key technologies in the proposed method are introduced in the following three parts:

$$v_{\mathrm{GS(4pin)}} = v_{\mathrm{GS(M)}} - i_{\mathrm{G}} \cdot R_{\mathrm{G(int)}} - (L_{\mathrm{G}} + L_{\mathrm{KS}}) \cdot \mathrm{d}i_{\mathrm{G}}/\mathrm{d}t \quad (14)$$

$$v_{\mathrm{GS(3pin)}} = v_{\mathrm{GS(M)}} - i_{\mathrm{G}} \cdot R_{\mathrm{G(int)}} - (L_{\mathrm{G}} + L_{\mathrm{S}}) \cdot \mathrm{d}i_{\mathrm{G}}/\mathrm{d}t - L_{\mathrm{S}} \cdot \mathrm{d}i_{\mathrm{DS}}/\mathrm{d}t. \quad (15)$$

A. i_{G} and i_{DS} Measurement

The first step to implement the proposed method is to measure i_{G} and i_{DS} by constructing DPT. As described in (14) and (15), only i_{G} affects the v_{GS} measurement of TO-247-4 devices, whereas both i_{G} and i_{DS} affect that of TO-247-3 devices. i_{DS} measurement is commonplace and implemented well enough by a shunt resistor with a passive probe. It is noted that this method can only measure the i_{DS} of the lower switch in the half-bridge since the shunt resistor should keep connected common grounding with the passive probe. It is also the reason that the higher switch is driven and crosstalk on the lower one is measured.

However, it is not suitable to measure i_{G} by shunt resistor with a passive probe due to the grounding issue of probes. A sampling resistor with a differential probe is preferred, with the benefit of directly using the drive resistor as the sampling resistor, as long as the voltage range is matched. To realize a high common-mode rejection ratio in the high-frequency range [5], the low-voltage optical isolation probe is selected as the substitution for the differential probe.

B. $\mathrm{d}i_{\mathrm{G}}/\mathrm{d}t$ and $\mathrm{d}i_{\mathrm{DS}}/\mathrm{d}t$ Calculation

Besides i_{G} and i_{DS}, their variation also induces measurement deviation, and $\mathrm{d}i_{\mathrm{G}}/\mathrm{d}t$ and $\mathrm{d}i_{\mathrm{DS}}/\mathrm{d}t$ are extracted from measured waveforms by the numerical differentiation method. Since waveforms are sampled at equal intervals, the numerical differentiation result can be regarded as the derivative of an interpolating polynomial. In other words, the derivative value corresponding to the sample point can be expressed by a linear combination of values of adjacent sample points. Here, the five-point method is selected for better accuracy, and the derivative value on the kth sample point DP_k is calculated by (16) with a truncation error proportional to h^4, where P_k is the value of the kth sample point and h is the sample interval. When the sampling frequency is high enough, the accuracy of the numerical differentiation is guaranteed. In the case given in this article, the sampling frequency is set as 12.5 GHz

$$DP_k = \frac{-P_{k+2} + 8P_{k+1} - 8P_{k-1} + P_{k-2}}{12h}. \quad (16)$$

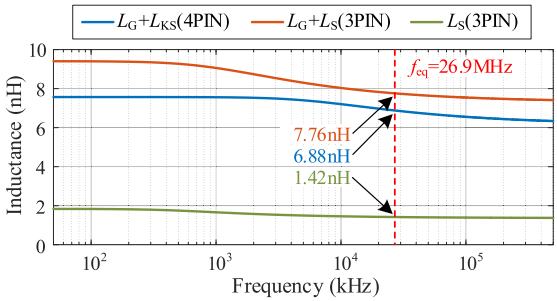

Fig. 12. Parasitic inductances with different frequencies.

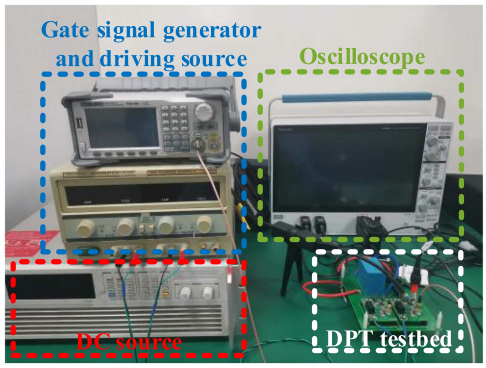

Fig. 13. Double pulse test experimental setup.

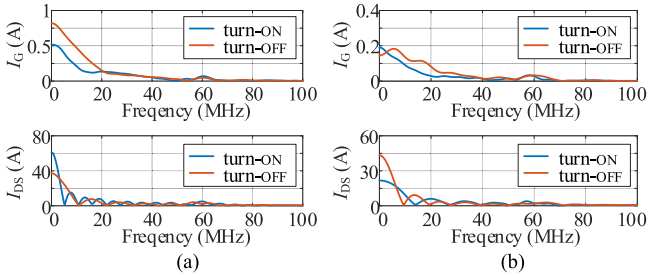

Fig. 14. FFT results of i_G and i_{DS} ($I_L = 40$ A, $R_{G(ext)} = 5\ \Omega$). (a) Switching process. (b) Crosstalk.

C. Parasitic Parameter Extraction

After waveform measuring, parasitic parameters causing v_{GS} measurement deviation should be extracted. To eliminate the impact of parasitic parameters on v_{GS} measurement, probes are as close to the root of pins as they can be, and parasitic parameters caused by the package are mainly considered [5], [28]. As shown in Fig. 3, they are L_G and L_{KS} in TO-247-4 devices, and L_G and L_S in TO-247-3 devices. One commonly used solution is finite element analysis by software such as ANSYS Q3D. Packages are modeled according to the datasheet and the parasitic inductances are obtained by setting imaginary sources and sinks. It is noted that these inductances are strongly affected by the lead length [7], [29] and should be extracted at the root of the leads.

According to the frequency sweeping results shown in Fig. 12, these inductances are frequency sensitive, making the calculation of voltage drops complicated. A general solution is to consider these inductances as linear systems. Based on the analysis in the frequency domain, the voltage drops equal the product of their transfer functions $L_x(s)$ and the corresponding current differentiations $DI_x(s)$, as shown in (17). And then, the time-domain representation of the voltage drops is obtained by the inverse Fourier transform. Moreover, in this way, it is convenient to calculate current differentiation in the frequency domain as (18), where $I_x(s)$ is the corresponding current

$$V_x(s) = L_x(s) \cdot DI_x(s) \tag{17}$$

$$V_x(s) = sL_x(s) \cdot I_x(s). \tag{18}$$

However, the former general solution is complicated and can be further simplified, since these inductances vary slightly with frequency. Some studies have eliminated these parasitic parameters with acceptable accuracy by waveforms [30], where the rising and falling durations of i_{DS} are utilized. According to the effective bandwidth of rising and falling i_{DS} slopes expressed based on the signal theory [31], the equivalent frequency of the switching process ($f_{eq} = 26.9$ MHz) is calculated by (19), where t_r and t_f are the rising and falling time. Thus, parasitic parameters when $R_{G(ext)}$ is 5 Ω are pointed out in Fig. 12. Based on the simplified solution, the frequency-domain analysis is canceled, and the numerical differentiation method is preferred for di_G/dt and di_{DS}/dt calculation

$$f_{eq} = \max\left(\frac{0.35}{t_r}, \frac{0.35}{t_f}\right). \tag{19}$$

The intrinsic gate resistance $R_{G(int)}$ also strongly affects v_{GS} measurement, which is an equivalent resistance due to device structure contributions such as oxide and P-body [32]. It can be easily measured by power device analyzers such as B1506A. Usually, the SiC MOSFET datasheet also gives it for reference. It is noted that the parasitic resistance induced by packages is too much less than $R_{G(int)}$ to be ignored.

V. Experimental Verification and Discussion

The DPT experiment is constructed to verify the measuring v_{GS} deviation analysis and the proposed v_{GS} extraction method. As shown in Fig. 13, the testbed operates under $V_{Bus} = 800$ V, $V_{DRV(ON)} = 18$ V, $V_{DRV(OFF)} = -5$ V, and $L = 500\ \mu$H. The type of MOSFETs is IMZ120R045M1. To eliminate errors induced by the test equipment, TPP1000, a 10x passive probe with 1 GHz bandwidth, is adopted for v_{GS} measurement; TPP0850, a 50x passive probe with 800 MHz bandwidth, is adopted for v_{DS} measurement; and TIVP1L, a 10x optical isolation probe with 1 GHz bandwidth, is adopted for i_G measurement by measuring the voltage on the external driving resistance $R_{G(ext)}$. Further analysis reveals the relationship between designed parameters, such as I_L and $R_{G(ext)}$, and the measurement deviation.

A. Voltage Drop Extraction Verification

The simplified solution for extracting voltage drops (v_{Drop}) on parasitic parameters is firstly verified. According to the fast Fourier transform (FFT) shown in Fig. 14, the main component of i_G and i_{DS} is less than 40 MHz. Since parasitic inductances are frequency-sensitive in this range, the frequency domain

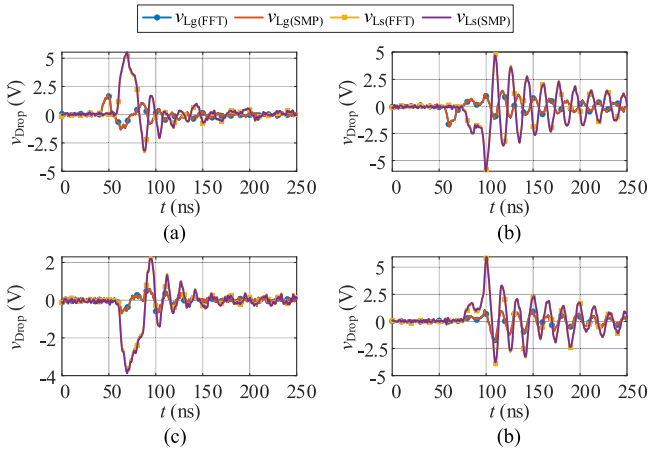

Fig. 15 v_{Drop} calculation results based on FFT and simplified (SMP) method ($I_{\mathrm{L}} = 40$ A, $R_{\mathrm{G(ext)}} = 5\ \Omega$). (a) Switching ON (b) Switching OFF. (c) Crosstalk ON. (b) Crosstalk OFF.

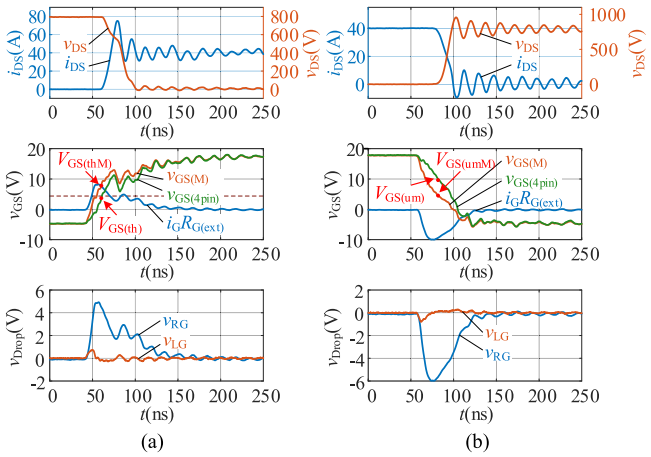

Fig. 16. Switching process experimental results of the TO-247-4 device ($I_{\mathrm{L}} = 40$ A, $R_{\mathrm{G(ext)}} = 5\ \Omega$). (a) Turn ON. (b) Turn OFF.

solution for parasitic inductance extraction is compared with the simplified one. As shown in Fig. 15, the simplified solution guarantees accurate v_{Drop} calculation without complicated frequency domain calculation. $\mathrm{d}i_{\mathrm{G}}/\mathrm{d}t$ and $\mathrm{d}i_{\mathrm{DS}}/\mathrm{d}t$ are obtained by the numerical differentiation in the simplified solution.

B. Switching Process Verification and Discussion

Switching process waveforms with $I_{\mathrm{L}} = 40$ A are measured, as shown in Figs. 16 and 17. The measured v_{GS} ($v_{\mathrm{GS(M)}}$) varies faster than the extracted v_{GS} ($v_{\mathrm{GS(4pin)}}$/$v_{\mathrm{GS(3pin)}}$) during stages of rapid changing, which is the common feature for both the TO-247-4 and TO-247-3 devices. Comparing v_{RG} and v_{LG}, the main effect caused by driving circuit behavior is reflected in i_{G} rather than $\mathrm{d}i_{\mathrm{G}}/\mathrm{d}t$. Besides, the TO-247-3 package induces a dramatic v_{LS} caused by the power circuit behavior $\mathrm{d}i_{\mathrm{DS}}/\mathrm{d}t$. Thus, a larger $v_{\mathrm{GS(M)}}$ peak during the turn-ON process and larger $v_{\mathrm{GS(M)}}$ oscillations are measured. The experimental results are consistent with the analysis and simulation.

The threshold voltage ($V_{\mathrm{GS(th)}}$) is selected to quantify the measurement deviation and the validity of the improved method.

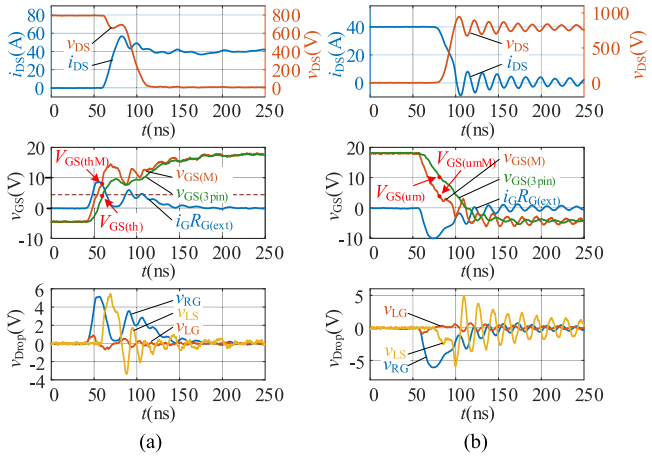

Fig. 17. Switching process experimental results of the TO-247-3 device ($I_{\mathrm{L}} = 40$ A, $R_{\mathrm{G(ext)}} = 5\ \Omega$). (a) Turn ON. (b) Turn OFF.

TABLE I
COMPARISON BETWEEN MEASURED $V_{\mathrm{GS(TH)}}$ WITH REFERENCE

Package	Reference	Conventional Method		Improved Method	
	$V_{\mathrm{GS(th0)}}$ (V)	$V_{\mathrm{GS(thM)}}$ (V)	$\Delta V_{\mathrm{GS(thC)}}$ (V)	$V_{\mathrm{GS(th)}}$ (V)	$\Delta V_{\mathrm{GS(thI)}}$ (V)
TO-247-4	4.50	8.83	4.33	4.58	0.08
TO-247-3	4.50	10.44	5.94	4.70	0.20

TABLE II
COMPARISON BETWEEN MEASURED AND REAL $V_{\mathrm{GS(UM)}}$

Package	$V_{\mathrm{GS(umM)}}$ (V)	$V_{\mathrm{GS(um)}}$ (V)	$\Delta V_{\mathrm{GS(um)}}$ (V)
TO-247-4	4.24	9.64	-5.40
TO-247-3	3.29	9.99	-6.70

Here, $V_{\mathrm{GS(th)}}$ observed in the turn-ON waveforms is defined as v_{GS} at which i_{DS} starts rising from zero. The reference $V_{\mathrm{GS(th0)}}$ is obtained by static characterization, which is in brown dash lines in Figs. 16 and 17. Table I illustrates that $V_{\mathrm{GS(th)}}$ measured by the proposed method is close to the reference, whereas $V_{\mathrm{GS(thM)}}$ measured by the conventional method obviously deviates from it. Besides, the deviation between $V_{\mathrm{GS(th)}}$ and $V_{\mathrm{GS(thM)}}$ ($\Delta V_{\mathrm{GS(th)}}$) is used to quantify the v_{GS} measurement deviation during the turn-ON process.

The maximum underestimation ($\Delta V_{\mathrm{GS(um)}}$) is observed to quantify the v_{GS} measurement deviation during the turn-OFF process. $V_{\mathrm{GS(um)}}$ and $V_{\mathrm{GS(umM)}}$ are the measured v_{GS} and the extracted v_{GS} values where the deviation is greatest. The result in Table II shows that $\Delta V_{\mathrm{GS(um)}}$ is 5.40 V for the TO-247-4 device, whereas 6.70 V for the TO-247-3 device.

Furthermore, both the driving circuit design and the operating condition affect the measurement deviation. As analyzed in Section II, $R_{\mathrm{G(ext)}}$ affects the deviation by switching speed, whereas I_{L} affects it by the duration of the i_{DS}-varying process. Table III shows the effect of $R_{\mathrm{G(ext)}}$ during the switching process with $I_{\mathrm{L}} = 40$ A. The result shows that the reduction of $R_{\mathrm{G(ext)}}$ aggravates $\Delta V_{\mathrm{GS(th)}}$ and $\Delta V_{\mathrm{GS(um)}}$, consistent with the analysis and simulation in Section II. Thus, it is indicated that besides the EMI deterioration, blindly reducing $R_{\mathrm{G(ext)}}$ also aggravates measurement deviation. This is another reason why reducing $R_{\mathrm{G(ext)}}$ of TO-247-3 devices is not suitable to obtain

TABLE III
EFFECT OF $R_{G(EXT)}$ ON v_{GS} MEASUREMENT DURING SWITCHING PROCESS

$R_{G(ext)}$ (Ω)	TO-247-4		TO-247-3	
	$\Delta V_{GS(th)}$ (V)	$\Delta V_{GS(um)}$ (V)	$\Delta V_{GS(th)}$ (V)	$\Delta V_{GS(um)}$ (V)
2	6.55	-8.44	8.35	-9.56
5	4.25	-5.40	5.74	-6.70
10	2.61	-3.37	3.65	-3.86

TABLE IV
EFFECT OF I_L ON v_{GS} MEASUREMENT DURING SWITCHING PROCESS

I_L (A)	TO-247-4		TO-247-3	
	$\Delta V_{GS(th)}$ (V)	$\Delta V_{GS(um)}$ (V)	$\Delta V_{GS(th)}$ (V)	$\Delta V_{GS(um)}$ (V)
10	4.24	-4.68	5.67	-5.33
20	4.24	-4.97	5.54	-5.90
30	4.28	-5.24	5.64	-6.28
40	4.25	-5.40	5.74	-6.70

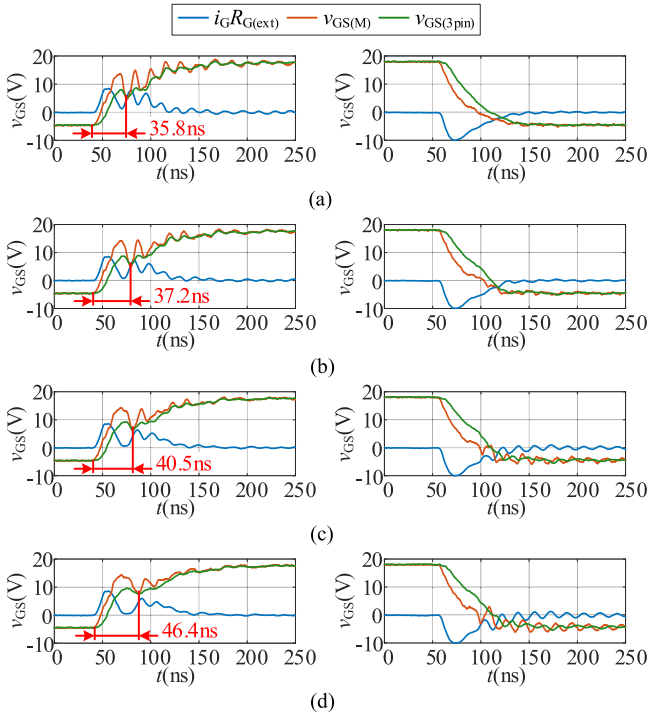

Fig. 18 Effect of I_L on deviation duration of TO-247-3 switching process. (a) $I_L = 10$ A, turn ON and OFF. (b) $I_L = 20$ A, turn ON and OFF. (c) $I_L = 30$ A, turn ON and OFF. (d) $I_L = 40$ A, turn ON and OFF.

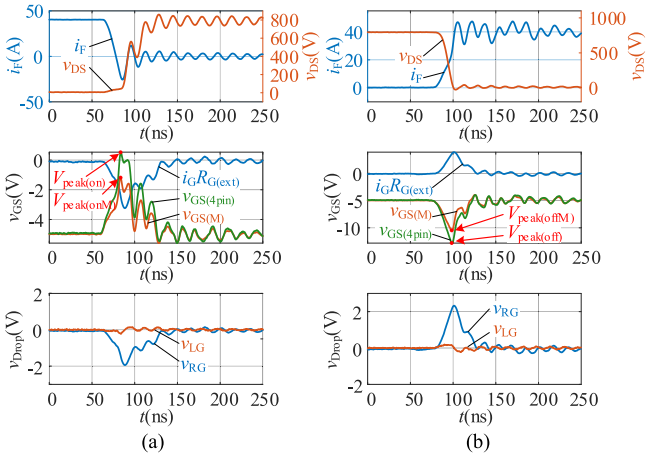

Fig. 19. Crosstalk experimental results of the TO-247-4 device ($I_L = 40$A, $R_{G(ext)} = 5\ \Omega$). (a) Turn ON (b) Turn OFF.

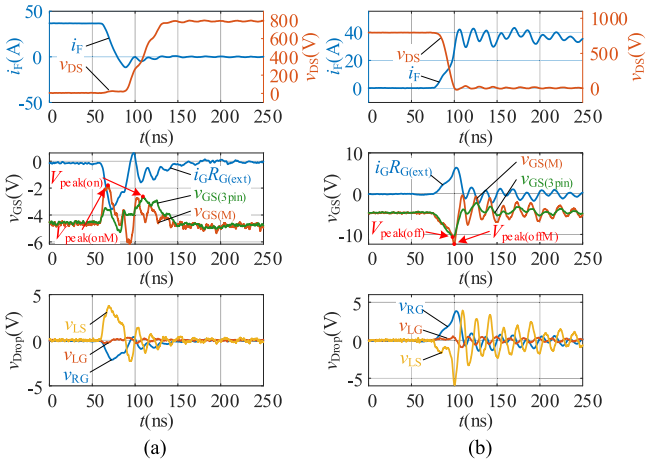

Fig. 20. Crosstalk experimental results of the TO-247-3 device ($I_L = 40$ A, $R_{G(ext)} = 5\ \Omega$). (a) Turn ON. (b) Turn OFF.

TABLE V
COMPARISON BETWEEN MEASURED AND REAL $V_{PEAK(ON)}$

Package	$V_{peak(onM)}$ (V)	$V_{peak(on)}$ (V)	$\Delta V_{p(on)}$ (V)
TO-247-4	-1.16	0.53	-1.69
TO-247-3	-1.85	-2.67	0.82

as high switching speed and low switching energy as TO-247-4 devices, as a supplement of [28].

The effect of I_L on deviations during the switching process with $R_{G(ext)} = 5\ \Omega$ is shown in Table IV. $|\Delta V_{th(ON)}|$ is hardly affected since no matter what the value of I_L is, i_{DS} is always 0 A when v_{GS} reaches $V_{GS(th)}$. $|\Delta V_{GS(um)}|$ slightly increases when I_L increases, since the maximum measured deviation occurs with a large i_{DS} determined by I_L. For the TO-247-3 device, the increased I_L extends the duration with an obvious deviation during the turn-ON process, and amplifies oscillation amplitude deviation during the turn-OFF process, as shown in Fig. 18.

The switching speed requirement limits the utility of large $R_{G(ext)}$, and I_L is determined by converter operating conditions. The restricted parameter selection makes it necessary to suppress the measurement deviation by the proposed method, especially for TO-247-3 package devices operating in high-capacity converters.

C. Crosstalk Verification and Discussion

Crosstalk waveforms with $I_L = 40$ A are measured, as shown in Figs. 19 and 20. The experimental results are consistent with the analysis and simulation. For the TO-247-4 device, the amplitude of $v_{GS(M)}$ peak during both turn-ON and turn-OFF crosstalk ($V_{peak(ON)}$ and $V_{peak(OFF)}$) are obviously underestimated. Comparing v_{RG} and v_{LG}, the main effect caused by driving circuit behavior is reflected in i_G rather than di_G/dt. It causes 1.69 V and 2.28 V underestimation of $V_{peak(ON)}$ and $V_{peak(OFF)}$,

TABLE VI
COMPARISON BETWEEN MEASURED AND REAL $V_{\mathrm{PEAK(OFF)}}$

Package	$V_{\mathrm{peak(offM)}}$ (V)	$V_{\mathrm{peak(off)}}$ (V)	$\Delta V_{\mathrm{p(off)}}$ (V)
TO-247-4	-10.52	-12.80	2.28
TO-247-3	-12.41	-10.66	-1.75

TABLE VII
EFFECT OF $R_{\mathrm{G(EXT)}}$ ON v_{GS} MEASUREMENT DURING CROSSTALK

$R_{\mathrm{G(ext)}}$ (Ω)	TO-247-4		TO-247-3		
	$\Delta V_{\mathrm{p(on)}}$ (V)	$\Delta V_{\mathrm{p(off)}}$ (V)	$\Delta V_{\mathrm{p(on)}}$ (V)	$\Delta V_{\mathrm{p(off)}}$ (V)	ΔV_{os} (V)
2	-3.12	-2.96	2.79	0.42	4.99
5	-1.69	-2.28	0.82	-1.75	3.73
10	-1.11	-1.43	0.10	-2.26	2.67

TABLE VIII
EFFECT OF I_{L} ON v_{GS} MEASUREMENT DURING CROSSTALK

I_{L} (A)	TO-247-4		TO-247-3		
	$\Delta V_{\mathrm{p(on)}}$ (V)	$\Delta V_{\mathrm{p(off)}}$ (V)	$\Delta V_{\mathrm{p(on)}}$ (V)	$\Delta V_{\mathrm{p(off)}}$ (V)	ΔV_{os} (V)
10	-1.71	-0.99	0.62	0.13	1.10
20	-1.67	-1.72	0.34	0.47	1.59
30	-1.63	-2.07	0.76	-0.80	2.96
40	-1.69	-2.28	0.82	-1.75	3.73

respectively, as illustrated in Tables V and VI. $\Delta V_{\mathrm{p(ON)}}$ and $\Delta V_{\mathrm{p(OFF)}}$ are the deviation of v_{GS} peak amplitude.

Besides v_{RG} and v_{LG}, the TO-247-3 package induces a dramatic $\mathrm{d}i_{\mathrm{DS}}/\mathrm{d}t$ effect reflected in the oscillating v_{LS}. It changes the shape of the $v_{\mathrm{GS(M)}}$ waveform during the turn-ON crosstalk. Although the $v_{\mathrm{GS(M)}}$ peak amplitude is overestimated by only 0.82 V, an obvious $v_{\mathrm{GS(M)}}$ peak advance of about 38.36 ns is measured. During the turn-OFF crosstalk, although v_{LS} counteracts the measurement deviation caused by i_{G}, it still overestimates the $v_{\mathrm{GS(M)}}$ peak amplitude by 1.75 V.

The measurement deviation of crosstalk is also affected by $R_{\mathrm{G(ext)}}$ and I_{L}. Table VII shows the effect of $R_{\mathrm{G(ext)}}$ during the crosstalk with $I_{\mathrm{L}} = 40$ A. In particular, ΔV_{os} is extracted as the deviation of the maximum v_{GS} oscillation peak value during the turn-OFF crosstalk. The result shows that the reduction of $R_{\mathrm{G(ext)}}$ aggravates $\Delta V_{\mathrm{p(ON)}}$ and $\Delta V_{\mathrm{p(OFF)}}$ for the TO-247-4 device and $\Delta V_{\mathrm{p(ON)}}$ for the TO-247-3 device, but suppresses $\Delta V_{\mathrm{p(OFF)}}$ for the TO-247-3 device, which is caused by the growing v_{RG} who counteracts v_{LG}. $v_{\mathrm{GS(M)}}$ oscillation is also amplified, consistent with the analysis and simulation in Section III. Thus, it is indicated that $R_{\mathrm{G(ext)}}$ cannot be too small to eliminate the error of crosstalk evaluation, guiding crosstalk suppression methods such as the active miller clamp [28].

The effect of I_{L} ON deviations during the crosstalk with $R_{\mathrm{G(ext)}} = 5\ \Omega$ is shown in Table VIII. For the TO-247-4 device, $\Delta V_{\mathrm{p(ON)}}$ is hardly affected since the device is in the reverse recovery process at that moment, which is not determined by I_{L}. $\Delta V_{\mathrm{p(OFF)}}$ is slightly aggravated when I_{L} increases, since a large I_{L} corresponds to a high i_{G} to guarantee the charging of C_{iss}. However, for the TO-247-3 device, the increase of I_{L} corresponds to an increasing i_{F} oscillation, which makes the $\Delta V_{\mathrm{p(ON)}}$ and $\Delta V_{\mathrm{p(OFF)}}$ irregularly vary. The main effect of a larger I_{L} can be summarized as a longer v_{GS} peak advance during the turn-ON crosstalk, and a larger oscillation amplitude during the turn-OFF crosstalk, as illustrated in Fig. 21.

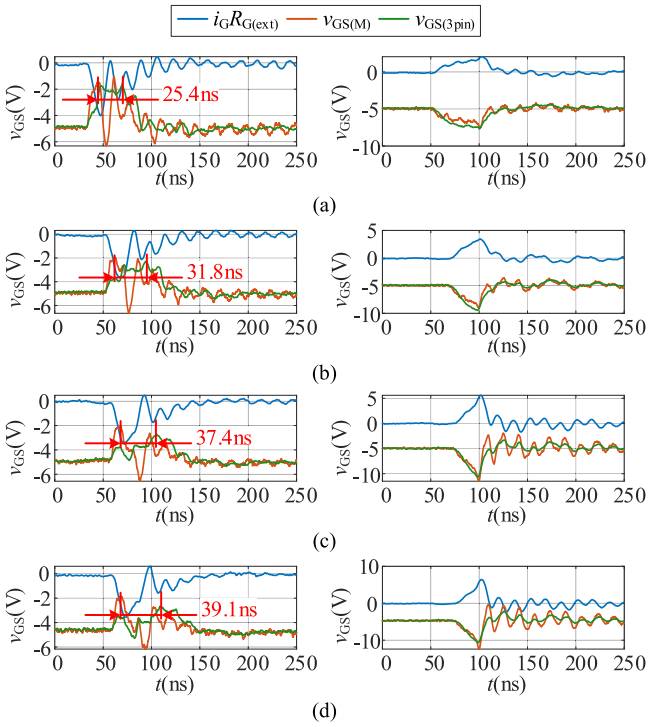

Fig. 21. Effect of I_{L} on deviation duration of TO-247-3 crosstalk. (a) $I_{\mathrm{L}} = 10$ A, turn ON and OFF. (b) $I_{\mathrm{L}} = 20$ A, turn ON and OFF. (c) $I_{\mathrm{L}} = 30$ A, turn ON and OFF. (d) $I_{\mathrm{L}} = 40$ A, turn ON and OFF.

In the commonly used half-bridge circuit, the upper and lower devices alternately play the role of the active device and its complementary device, and I_{L} is also determined by converter operating conditions. It means that the measurement deviation during the crosstalk also needs to be suppressed by the proposed method, especially for TO-247-3 package devices operating in high-capacity converters.

VI. CONCLUSION

In this article, the v_{GS} measurement deviation of the SiC MOSFET during the switching process and crosstalk is revealed. The v_{GS} on the chip is identified as the measuring object based on the equivalent circuit model. Simulation waveforms illustrate the v_{GS} measurement deviation caused by parasitic parameters between measuring points. For the switching process, the measuring result overestimates the v_{GS} change rate during the turn-ON and turn-OFF process, which is more severe for TO-247-3 devices. For the crosstalk, the measuring result underestimates the v_{GS} peak amplitude of TO-247-4 devices and misjudges both peak amplitude and emerging stage of TO-247-3 devices. These inaccurate v_{GS} measuring waveforms mislead devices' characterization and evaluation, incurring additional costs of the driving circuit and possible invalidation of crosstalk suppression in practice.

An accurate v_{GS} on the chip extraction method is proposed. The parasitic parameter impact is compensated with the help of high-precision measurement equipment and the proven parasitic parameter extraction technique. The DPT experiment validates the deviation elimination effectiveness of

this method. Furthermore, exploration of different operating conditions including $R_{G(ext)}$ and I_L quantifies their effect on the measurement deviation and the necessity of this method. The restricted $R_{G(ext)}$ and I_L selection make it necessary to eliminate the measurement deviation, especially for TO-247-3 devices operating in high-capacity converters and devices with a small external driving resistance. The proposed method and conclusion are applicable to other types of packages.

This article contributes to the understanding of measurement for power semiconductor devices, especially wide band-gap devices. Besides the precision improved by equipment and techniques, accurate measurement requires a clear measuring object. The proposed v_{GS} measurement deviation model and elimination method complement previous studies and deserve to be applied in device research and development for more rigorous verification and evaluation.

REFERENCES

[1] F. Wang, Z. Zhang, and E. A. Jones, *Characterization of Wide Bandgap Power Semiconductor Devices*. London, U.K.: Institution Eng. Technol., 2018.

[2] X. She, A. Q. Huang, Ó. Lucía, and B. Ozpineci, "Review of silicon carbide power devices and their applications," *IEEE Trans. Ind. Electron.*, vol. 64, no. 10, pp. 8193–8205, Oct. 2017.

[3] J. Millán, P. Godignon, X. Perpiñà, A. Pérez-Tomás, and J. Rebollo, "A survey of wide bandgap power semiconductor devices," *IEEE Trans. Power Electron.*, vol. 29, no. 5, pp. 2155–2163, May 2014.

[4] Z. Zhang, B. Guo, F. F. Wang, E. A. Jones, L. M. Tolbert, and B. J. Blalock, "Methodology for wide band-gap device dynamic characterization," *IEEE Trans. Power Electron.*, vol. 32, no. 12, pp. 9307–9318, Dec. 2017.

[5] Y. Gao and Q. Chen, *Silicon Carbide Power Semiconductor Devices: Characteristics, Testing and Applications*. Beijing, China: China Machine Press, 2021.

[6] J. B. Witcher, *Methodology For Switching Characterization of Power Devices and Modules*. Blacksburg, VA, USA: Virginia Polytechnic Inst. State Univ., 2003.

[7] C. Zhen, *Characterization and Modeling of High-Switching-Speed Behavior of SiC Active Devices*. Blacksburg, VA, USA: Virginia Polytechnic Inst. State Univ., 2009.

[8] Tektronix Inc., "ABCs of probes primer," Applicat. Note, 2021, [Online]. Available: http://www.tektronix.com

[9] Keysight Technologies Inc., "Keysight DP0001A high voltage differential probe user's guide, applicat. Note," 2020. [Online]. Available: https://www.keysight.com

[10] Z. Zeng, J. Wang, L. Wang, Y. Yu, and K. Ou, "Inaccurate switching loss measurement of SiC MOSFET caused by probes: Modelization, characterization, and validation," *IEEE Trans. Instrum. Meas.*, vol. 70, pp. 1–14, Nov. 17, 2020.

[11] Z. Zeng, X. Zhang, and L. Miao, "Inaccuracy and instability: Challenges of SiC MOSFET transient measurement intruded by probes," in *Proc. 10th Int. Conf. Power Electron. ECCE Asia*, 2019, pp. 2139–2145.

[12] Z. Zeng, X. Zhang, F. Blaabjerg, and L. Miao, "Impedance-Oriented transient instability modeling of SiC MOSFET intruded by measurement probes," *IEEE Trans. Power Electron.*, vol. 35, no. 2, pp. 1866–1881, Feb. 2020.

[13] Tektronix Inc., "Probing techniques for accurate voltage measurements on power supplies with oscilloscopes," Applicat. Note, 2019. [Online]. Available: http://www.tektronix.com

[14] S. Li, *Packaging Design of IGBT Power Module Using Novel Switching Cells*. Knoxville, TN, USA: Univ. Tennessee, 2011.

[15] J. Wang, H. S. Chung, and R. T. Li, "Characterization and experimental assessment of the effects of parasitic elements on the MOSFET switching performance," *IEEE Trans. Power Electron.*, vol. 28, no. 1, pp. 573–590, Jan. 2013.

[16] F. Yang, Z. Wang, Z. Liang, and F. Wang, "Electrical performance advancement in SiC power module package design with Kelvin drain connection and low parasitic inductance," *IEEE J. Emerg. Sel. Topics Power Electron.*, vol. 7, no. 1, pp. 84–98, Mar. 2019.

[17] X. Li, L. Zhang, S. Guo, Y. Lei, A. Q. Huang, and B. Zhang, "Understanding switching losses in SiC MOSFET: Toward lossless switching," in *Proc. IEEE 3rd Workshop Wide Bandgap Power Devices Appl.*, 2015, pp. 257–262.

[18] Y. Ying, *Device Selection Criteria — Based on Loss Modeling and Figure of Merit*. Blacksburg, VA, USA: Virginia Polytechnic Inst. State Univ., 2008.

[19] Infineon Technologies A.G., "Coolmos^{TM} gate drive and switching dynamics," Applicat. Note, 2020. [Online]. Available: http://www.infineon.com

[20] D. Reusch and J. Strydom, "Understanding the effect of PCB layout on circuit performance in a high frequency gallium nitride based point of load converter," in *Proc. 28th Annu. IEEE Appl. Power Electron. Conf. Expo.*, 2013, pp. 649–655.

[21] S. Ji, S. Zheng, F. Wang, and L. M. Tolbert, "Temperature-Dependent characterization, modeling, and switching speed-limitation analysis of third-generation 10-kV SiC MOSFET," *IEEE Trans. Power Electron.*, vol. 33, no. 5, pp. 4317–4327, May 2018.

[22] H. Li, Y. Jiang, Z. Qiu, Y. Wang, and Y. Ding, "A predictive algorithm for crosstalk peaks of SiC MOSFET by considering the nonlinearity of gate-drain capacitance," *IEEE Trans. Power Electron.*, vol. 36, no. 3, pp. 2823–2834, Mar. 2021.

[23] S. Jahdi, O. Alatise, J. A. Ortiz Gonzalez, R. Bonyadi, L. Ran, and P. Mawby, "Temperature and switching rate dependence of crosstalk in Si-IGBT and SiC power modules," *IEEE Trans. Ind. Electron.*, vol. 63, no. 2, pp. 849–863, Feb. 2016.

[24] P. Wang, L. Zhang, X. Lu, H. Sun, W. Wang, and D. Xu, "An improved active crosstalk suppression method for high-speed SiC MOSFETs," *IEEE Trans. Ind. Appl.*, vol. 55, no. 6, pp. 7736–7744, Nov./Dec. 2019.

[25] Z. Zhang, F. Wang, L. M. Tolbert, and B. J. Blalock, "Active gate driver for crosstalk suppression of SiC devices in a phase-leg configuration," *IEEE Trans. Power Electron.*, vol. 29, no. 4, pp. 1986–1997, Apr. 2014.

[26] Y. Li, M. Liang, J. Chen, T. Q. Zheng, and H. Guo, "A low gate turn-OFF impedance driver for suppressing crosstalk of SiC MOSFET based on different discrete packages," in *IEEE J. Emerg. Sel. Topics Power Electron.*, vol. 7, no. 1, pp. 353–365, Mar. 2019.

[27] C. Li et al., "High off-state impedance gate driver of SiC MOSFETs for crosstalk voltage elimination considering common-source inductance," *IEEE Trans. Power Electron.*, vol. 35, no. 3, pp. 2999–3011, Mar. 2020.

[28] Y. Li, Y. Zhang, Y. Gao, S. Du, and J. Liu, "Switching characteristic analysis and application assessment of SiC MOSFET with common source inductance and Kelvin source connection," *IEEE Trans. Power Electron.*, vol. 37, no. 7, pp. 7941–7951, Jul. 2022.

[29] R. Bosshard, *Multi-Objective Optimization of Inductive Power Transfer Systems For EV Charging*. Zurich, Switzerland: ETH Zurich, 2015.

[30] S. K. Roy and K. Basu, "Measurement of important circuit parasitics for switching transient analysis of SiC MOSFET and schottky diode pair," in *Proc. IEEE Energy Convers. Congr. Expo.*, 2019, pp. 1948–1952.

[31] H. W. Johnson and M. Graham, *High-Speed Digital Design: A Handbook of Black Magic*. Englewood Cliffs, NJ, USA: Prentice-Hall, 1993.

[32] STMicroelectronics Inc., "Power MOSFET: RG impact on applications," Applicat. Note, 2012. [Online]. Available: http://www.st.com

Yang Li (Student Member, IEEE) received the B.S degree in 2019 from Xi'an Jiaotong University, Xi'an, China, where he is currently working toward the Ph.D. degree both in electrical engineering.

His research interests include reliability assessment and optimization design of power semiconductor devices and power electronic equipment.

Yuan Gao received the B.S. and M.S. degrees in electrical engineering from Xi'an Jiaotong University, Xi'an, China, in 2012 and 2015, respectively.

He is currently the Director of Application Test Center, Global Power Technology Company Ltd., Beijing, China, senior Member of Power Electronics Committee, China Electrotechnical Society (CES), the Industry Mentor of China Advanced Semiconductor Industry Innovation Alliance (CASA), and External Expert in power supply devices field of Tektronix Inc.

He is mainly engaged in the key technology research of power semiconductor devices characterization, evaluation and application, and is committed to promoting the popularization of power semiconductor device education in universities and the application of advanced power devices in the industry. He has published eight academic papers and holds four patents. His monograph "Silicon Carbide Power Devices: Characteristics, Testing and Application Technology" has been included in the "14th Five-Year Plan" national key publications.

Yan Zhang (Member, IEEE) received the Ph.D. degree in electrical engineering from Xi'an Jiaotong University (XJTU), Xi'an, China, in 2014.

He is currently an Associate Professor with the School of Electrical Engineering, XJTU. From 2016 to 2017, he was a Postdoctoral Research Fellow with the Department of Electrical and Computer Engineering, Queen's University, Kingston, ON, Canada. He has presided over research projects of the National Natural Science Foundation, China Postdoctoral Science and Province Foundation, and State Key Lab Foundation. He has authored or coauthored more than 100 technical papers in peer reviewed journals and conference proceedings and holds 10 China issued invention patents. His research interests include topology, model and control of power electronic systems, high-efficiency resonant power converters, and power electronics equipment reliability.

Jinjun Liu (Fellow, IEEE) received the B.S. and Ph.D. degrees in electrical engineering from Xi'an Jiaotong University (XJTU), Xi'an, China, in 1992 and 1997, respectively.

He was a faculty with the School of Electrical Engineering, XJTU. From late 1999 to early 2002, he was with the Center for Power Electronics Systems, Virginia Polytechnic Institute and State University, Blacksburg, VA, USA, as a Visiting Scholar. In late 2002, he was a Full Professor and then the Head of the Power Electronics and Renewable Energy Center, XJTU, which now comprises more than 20 faculty members and more than 200 graduate students and carries one of the leading power electronics programs in China. From 2005 to early 2010, he was an Associate Dean with the School of Electrical Engineering, XJTU, and from 2009 to early 2015, the Dean for Undergraduate Education of XJTU. He is currently a XJTU Distinguished Professor of Power Electronics. He coauthored 3 books (including one textbook), authored and coauthored more than 500 technical papers in peer-reviewed journals and conference proceedings, holds more than 70 invention patents (China/US/Europe), and delivered for many times plenary keynote speeches and tutorials at IEEE conferences or China national conferences in power electronics area. His research interests include modeling, control, and design methods for power converters and electronified power systems, power quality control and utility applications of power electronics, and microgrids for sustainable energy and distributed generation.

Dr. Liu was the recipient of many times governmental awards at national level or provincial/ministerial level for scientific research/teaching achievements. He was also the recipient of the 2006 Delta Scholar Award, the 2014 Chang Jiang Scholar Award, the 2014 Outstanding Sci-Tech Worker of the Nation Award, the 2016 State Council Special Subsidy Award, IEEE TRANSACTIONS ON POWER ELECTRONICS 2016 and 2021 Prize Paper Awards, the Nomination Award for the Grand Prize of 2020 Bao Steel Outstanding Teacher Award, and the 2022 Fok Ying Tung Education and Teaching Award. He was the IEEE Power Electronics Society Region 10 Liaison and then China Liaison for ten years. Since 2006, he has been an Associate Editor for the IEEE TRANSACTIONS ON POWER ELECTRONICS, 2015–2019 Executive Vice President and 2020–2021 Vice President of IEEE Power Electronics Society. He was on the Board of China Electrotechnical Society 2012–2020 and was elected the Vice President in 2013 and the Secretary General in 2018 of the CES Power Electronics Society. He was the Vice President for International Affairs, China Power Supply Society from 2013 to 2021, and since 2016, the inaugural Editor-in-Chief of CPSS Transactions on Power Electronics and Applications. He was elected the President of CPSS in November 2021. Since 2013, he has been the Vice Chair of the Chinese National Steering Committee for College Electric Power Engineering Programs.

Cheng Nie (Member, IEEE) was born in Hubei, China, in 1985. He received the B.S. degree in electrical engineering from Hunan University, Changsha, China, in 2008, and the M.S. and Ph.D. degrees in electrical engineering from Xi'an Jiaotong University, Xi'an, China, in 2011 and 2018, respectively, all in electrical engineering.

From 2019 to 2021, he was with the University of Tennessee, Knoxville, TN, USA, as a Postdoctoral Research Associate. Since 2021, he has been a System Engineer with the TBEA Xi'an Electric Technology Co. Ltd., Xi'an, China. His research interests include wide bandgap devices, modular multilevel converters, solid-state transformers, microgrids, and renewable energy.